PCCP

Accepted Manuscript

ROYAL SOCIETY OF CHEMISTRY

www.rsc.org/pccp

Double Hysteresis Loops and Large Negative and Positive Electrocaloric Effects in Tetragonal Ferroelectrics

Hong-Hui Wu[1], Jiaming Zhu[1,2] and Tong-Yi Zhang[3*]

[1] Department of Mechanical and Aerospace Engineering, Hong Kong University of Science and Technology, Clear Water Bay, Kowloon, Hong Kong, China

[2] Center of Microstructure Science, Frontier Institute of Science and Technology, Xi'an Jiaotong University, Xi'an, 710054, China

[3] Shanghai University Materials Genome Institute and Shanghai Materials Genome Institute, Shanghai University, 99 Shangda Road, Shanghai 200444, China

Abstract

Phase field modelling and thermodynamic analysis are employed to investigate depolarization and compression induced large negative and positive electrocaloric effects (ECEs) in ferroelectric tetragonal crystalline nanoparticles. The results show that double-hysteresis loops of polarization versus electric field dominate at temperatures below the Curie temperature of the ferroelectric material, when the mechanical compression exceeds a critical value. In addition to the mechanism of pseudo-first-order phase transition (PFOPT), the double-hysteresis loops are also caused by the abrupt rise of macroscopic polarization from the *abc* phase to the *c* phase or the sudden fall of macroscopic polarization from the *c* phase to the *abc* phase, when temperature increases. This phenomenon is called the electric-field-induced-pseudo-phase transition (EFIPPT) in the present study. Similar to two types PFOPTs, the two types of EFIPPTs cause large negative and positive ECEs, respectively, and give the maximums in absolute values of negative and positive adiabatic temperature change (ATC ΔT). The temperature associated with the maximum in absolute value of negative ATC ΔT is lower than that with the maximum positive ATC ΔT. Both maximum absolute

*Corresponding author. Tel & Fax: +86-21-66136172, E-mail: zhangty@shu.edu.cn

values of ATC ΔTs changes with the variation magnitude of an applied electric field and depend greatly on the compression intensity.

Keywords: Double-hysteresis loops; Electric-field-induced-pseudo-phase-transition (EFIPPT), Electrocaloric effect; Tetragonal ferroelectrics; Phase field model

1. Introduction

Electrocaloric (EC) effect refers to the change in adiabatic temperature or in isothermal entropy of a dielectric material by varying an applied electric field.[1] Due to the significantly temperature-dependence of polarization, ferroelectric/antiferroelectric materials based on the perovskite-structured oxides possess the EC effect, which can be used to manufacture solid-state cooling devices for a broad range of applications such as on-chip cooling and temperature regulation for sensors or other electronic devices.[2-4] Traditionally, there exists two approaches to measure the adiabatic temperature change (ATC) ΔT: direct and indirect. As the applied electric field increases from an initial value E_α to a final value E_β, $\Delta T\left(\Delta E = \mathrm{E}_\beta - \mathrm{E}_\alpha\right)$ can be directly measured under adiabatic condition, which is extremely desirable and very challenging,[5] while the indirect approach is based on the Maxwell relation and ΔT, is calculated from

$$\Delta T = -\int_{E_\alpha}^{E_\beta} \frac{T}{C_E}\left(\frac{\partial P}{\partial T}\right)_E dE, \tag{1}$$

where C_E is the specific heat capacity per unit volume. In an ideal refrigeration cycle basing on the extensively reported conventional EC effect,[6-9] both isothermal entropy change (IEC) ΔS and the ATC ΔT are key parameters to gauge the EC effect of a ferroelectric/antiferroelectric material.

To schematically illustrate the conventional thermodynamic cycle of EC materials, we replace mechanical pressure and volume by electric voltage and electric charge, respectively, in analogy to the classical inversed Carnot cycle. Electric voltage and electric charge are further reduced, respectively, to electric field and electric displacement (or polarization), so that Eq. (1) becomes relevant. The electric field versus polarization and entropy versus temperature are plotted in Fig. 1(A) and (B), respectively. As shown, from the path of (a) to (b), an applied electric field is adiabatically raised from E_α to E_β and the EC material experiences an adiabatic temperature change ΔT from T_1 to T_2. Then from the path of (b) to (c), the applied electric field is isothermally increased, the EC material releases heat (entropy) to the heat sink at T_2 while the material entropy is reduced from S_2 to S_1 (IEC ΔS). From the path of (c) to (d), the applied electric field is adiabatically reduced and the EC material experiences a decrease in temperature from T_2 to T_1. At temperature T_1 or from (d) to (a), the applied electric field is isothermally decreases and the EC material isothermally absorbs heat (entropy) from the cold sink. After that, a thermodynamic cycle is completed and the EC material returns its initial state (a). Because the EC materials of interest are insulators, the above electric field (refrigeration) cycle has the potential of very low electric loss and consequently, the cooling devices based on the EC effect have the potential to reach very high efficiency.

EC materials attracted scientific interest in the 1960s and 1970s.[1-4,10] At that time, the EC effect was not high enough for practical applications that low electric fields induced only a small change in ATC (ΔT <2 K). The research interest of EC effect has been revived since 2006,[11] when 350-nm-thick sol-gel films of the ceramic $PbZr_{0.95}Ti_{0.05}O_3$ showed a large value of ΔT = 12 K, in response to relatively large value of ΔE = 480 kV cm^{-1} near the Curie temperature of 495 K. A

similar value of ΔT = 12.5 K was reported for the ~1-μm-thick spin-cast polymer film[12] of the ferroelectric poly(vinylidene fluoride–trifluoroethylene) (P(VDF-TrFE)) 55/45 mol % copolymer, driven by ΔE = 2090 kV·cm^{-1} at temperature 353 K. After that, the large EC effect has been observed in many ferroelectric, antiferroelectric, and relaxor thin films,[13-18] mainly because thin films can tolerate higher electric fields without breakdown. Since the EC effect in ferroelectric, antiferroelectric, and relaxor materials is directly related to polarization changes under varying electric field, a large polarization change is highly desirable to achieve a large EC effect. Near the first-order paraelectric/ferroelectric transition (FOPFT) Curie temperature, a switching from ferroelectric phase to paraelectric phase makes the EC effect largest.[17,19-24] For example, the temperature change ΔT of poly (vinyledene fluoride–trifluoroethylene) (P(VDF–TrFE)) 55/45 mol% copolymers was directly measured over a broad temperature range using a specially designed calorimetry method.[17] The data revealed a large EC effect occurring at the ferroelectric-paraelectric (FE-PE) phase transition where a temperature increase ~12 °C was induced under an electric field change of 120 MV/m. Moya *et al.*[24] performed direct measurement of the electrically driven temperature change ΔT in single crystal $BaTiO_3$ and found the giant EC strength $\Delta T / \Delta E$ =0.22 K·cm·kV^{-1} near the phase transition Curie temperature T_c.

The EC effect is positive if the adiabatic temperature of a ferroelectric/antiferroelectric material increases, when an applied field increases from a low strength or zero to a high strength. Otherwise, the EC effect is negative. Although most of EC effects in ferroelectric/antiferroelectric materials were found to be positive in the past decades, an optimized cooling cycle is to utilize both positive and negative EC effects. Fortunately, the negative EC effect has been observed in antiferroelectric/ferroelectric materials recently.[25-36] Antiferroelectrics (AFEs) are characterized by

an antipolar crystal structure with two (or more) spontaneous polarizations of opposite directions in a crystalline lattice and manifest the zero macroscopic spontaneous polarization and the induced antiferroelctric-to-ferroelectric phase transition by high-enough electric field. In contrast to normal ferroelectric materials, the field induced macroscopic polarization versus electric field in AFEs shows a typical double-hysteresis loop after a linear stage and renders abnormal EC effects to AFEs. For instance, Geng *et al*.[35] fabricated a typical antiferoelectric $(Pb_{0.97}La_{0.02})(Zr_{0.95}Ti_{0.05})O_3$ thin films on a $Pt(111)/Ti/SiO_2/Si$ substrate by using sol-gel spin-coating. They observed a maximum of negative ΔT, called negative ΔT peak hereafter, for each applied electric field change ΔE. The negative ΔT peak shifted its position toward lower temperature as ΔE increased, and meanwhile increased its magnitude. Interestingly, a giant negative EC effect was clearly demonstrated with a maximum amplitude value of -5.76 K at 59 °C under an applied field change of ΔE=338 kV·cm^{-1} ($E_\beta \approx$415 kV·cm^{-1}).[35] When E_β further increased, a significant reduction of the negative $|\Delta T|$ was observed. This was due to the field-induced conventional (or positive) EC effect that compensated the negative EC effect. Using atomistic first-principles based simulations of the EC effect in $Ba_{0.5}Sr_{0.5}TiO_3$ alloy, Ponomareva and Lisenkov[27] found that ferroelectrics with multiple phase transitions could exhibit a giant ECE by a large change in electric field and the coexistence of both positive and negative ECE in one material. Fig. 3(a) in Reference [27] illustrates that the average polarization component $\langle P_3 \rangle$ under an electric field of 300 kV/cm applied along the [001] direction increases with temperature near the phase transition temperature 155 K, which will give negative EC effect. The advent of negative EC effect enlarges the EC family and enhances the cooling efficiency when combined with positive EC effect. However, the underlying mechanism of the negative EC effect is still elusive. The temperature-dependent hysteresis measurement[36] on

lead-free $Sr_xBa_{(1-x)}Nb_2O_6$ (x=0.50, 0.61 and 0.75) ferroelectric single crystals revealed that the spontaneous polarization of the single crystals decreased with the decrease in temperature, when the temperatures were below the critical temperature T_{max} at which the dielectric constant is a maxima. As a consequence, these crystals exhibited negative and positive EC effects at temperatures lower and above T_{max}, respectively. Obviously, more experimental and theoretical investigations are needed to clarify the mechanism of negative EC effect.

Our previous work[37,38] proposes a novel concept of pseudo-first-order phase transition (PFOPT) based on remnant polarization. It is well known that as temperature increases to Curie temperature, spontaneous polarization **P** drops from a finite value to zero, which is called FOPFT, Note that spontaneous polarization means polarization **P** without any applied electric field. In analogy, the phenomenon that remnant polarization drops from a finite value to zero is defined as type-I PFOPT, when temperature increases to the type-I PFOPT temperature.[37,38] Our previous work[38] also found another type of PFOPT, named type-II PFOPT, to describe the phenomenon that remnant polarization jumps from zero to a finite value, when temperature increases to type-II PFOPT temperature. In general, type-II PFOPT temperature is lower than type-I PFOPT temperature and type-I PFOPT temperature is lower than Curie temperature. Following the previous work,[37, 38] the present study introduces an innovative concept of electric-field-induced-pseudo-phase-transition (EFIPPT) based on phase transition between the *abc* phase and the *c* phase, which is described in detail in the following sections.

2. Methodology

Based on the Landau-Devonshire theory[39-41] of the ferroelectric phase transition and domain evolution, polarization $\mathbf{P}=(P_1,P_2,P_3)$ is usually used as the order parameter. The Gibbs free energy density under external constant field is given by

$$g\left(P_i,\sigma_{ij},E_i\right)=\alpha_i P_i^2+\alpha_{ij}^{\oplus}P_i^2P_j^2+\alpha_{ijk}P_i^2P_j^2P_k^2+\alpha_{ijkl}P_i^2P_j^2P_k^2P_l^2 -\frac{1}{2}s_{ijkl}\sigma_{ij}\sigma_{kl}-Q_{ijkl}\sigma_{ij}P_kP_l-E_iP_i \tag{2}$$

where α_i denotes the dielectric stiffness that is directly related to temperature via $\alpha_i=\left(T-T_0\right)/2\varepsilon_0C_0$, here T and T_0 are temperature and Curie-Weiss temperature, respectively, C_0 is the Curie constant, and ε_0 is the vacuum permittivity; $\alpha_{ij}^{\oplus}$, α_{ijj} and α_{ijjl} are higher order dielectric stiffnesses; s_{ij} are the elastic compliance coefficients; Q_{ij} are electrostrictive constants; σ_{ij} denote mechanical stress tensor; and E_i is external electric field. Note the depolarization field and self-energy of the external electric field are not considered in Eq. (2). The Gibbs free energy density is a function of polarization P_i, external mechanical load σ_{ij}, external electric field E_i, and temperature as well. Polarizations P_i and their combinations are called polarization variants or phases in the present work, which will be described below. Through the dielectric stiffness, temperature, as a scale, uniformly affects all polarizations P_i (i=1, 2, 3). External mechanical stress and electric field, as a tensor and a vector, respectively, may affect only some polarizations. In terms of polarization variants, every polarization variants contributes equally to the Gibbs free energy density if no mechanical stress and electric field are applied. With applied mechanical stress and electric field, some polarization variants will be larger than others and then they will contribute more to the Gibbs free energy, especially at the equilibrium state where the Gibbs free energy is minimized. In other words, applying and varying mechanical stress and electric

field will able to change the Gibbs free energy landscape with respect to polarizations and then change the phase transition among the polarization variants. Thus, selectively applying external fields of temperature, electric field, and stress field allows one to introduce multi-variants-phase transition in the ferroelectric tetragonal structure, which would greatly improve the performance of ferroelectric materials. In thermodynamic analysis, the studied system is assumed to be homogeneous so that the Gibbs energy density can used to express the energy landscape and estimate the phase transition among the polarization variants.

Differing from the homogeneous mono-domain assumption in the thermodynamic model, the free energy in phase field model is defined in terms of spatially continuous and heterogeneous polarization, where the energy penalty for spatially inhomogeneous polarization is explicitly considered as the polarization gradient energy. The domain configuration and polarization switching are a direct consequence of the minimization process of the total free energy over a whole simulated system,[42,43] which is a function of polarization, polarization gradient, strain and electric field. The free energy density is given by

$$f\left(P_i, P_{i,j}, \varepsilon_{ij}, E_i\right) = \alpha_i P_i^2 + \alpha_{ij} P_i^2 P_j^2 + \alpha_{ijk} P_i^2 P_j^2 P_k^2 + \alpha_{ijkl} P_i^2 P_j^2 P_k^2 P_l^2 + \frac{1}{2} c_{ijkl} \varepsilon_{ij} \varepsilon_{kl} - q_{ijkl} \varepsilon_{ij} P_k P_l + \frac{1}{2} G_{ijkl} P_{i,j} P_{k,l} - \frac{1}{2} \varepsilon_0 \varepsilon_b E_i E_i - E_i P_i \quad (i,\ j,\ k,\ l=1,\ 2,\ 3), \quad (3)$$

where the coefficient α_{ij} of the fourth order Landau-Devonshire energy term in Eq. (3) is different from $\alpha_{ij}^{\oplus}$ in Eq. (2) due to the change in independent variable from stress to strain, while coefficients α_i, α_{ijk}, α_{ijkl} in Eq. (3) are the same as that shown in Eq. (2). The fifth and sixth terms in Eq. (3) represent the mechanical energy of the system, where ε_{ij}, c_{ijkl}, and q_{ijkl} are the mechanical strain, elastic constant, and electrostrictive constants, respectively. The seventh term

denotes the gradient energy, where G_{ijkl} is the gradient coefficient and $P_{i,j}$ represents the spatial derivative of the i th component of the polarization vector, P_i, with respect to the j th coordinate. When a domain wall is treated as a diffuse boundary between two different polarization domains, the domain wall energy is obtained by integrating the gradient energy over the thickness of the diffuse domain wall. The last two terms are the electric energy density with the consideration of applied electric field and depolarization field, in which ε_b is background dielectric constant.

The temporal evolution of polarization is obtained through the time-dependent Ginzburg-Landau equation,

$$\frac{\partial P_i(\mathbf{x},t)}{\partial t} = -L\frac{\delta F}{\delta P_i(\mathbf{x},t)}, \tag{4}$$

where $F = \int_\Omega f\,dV$ is the total free energy of the studied system, L is a kinetic coefficient, t is time, $\frac{\delta F}{\delta P_i(\mathbf{x},t)}$ denotes the thermodynamic driving force, and $\mathbf{x}$ is the spatial vector $\mathbf{x}=(x_1,x_2,x_3)$. In addition to the governing equation (4) for polarization evolution, the following mechanical governing equation

$$\frac{\partial}{\partial x_j}\left(\frac{\partial f}{\partial \varepsilon_{ij}}\right) = 0, \tag{5}$$

and Gauss equation

$$\frac{\partial}{\partial x_i}\left(-\frac{\partial f}{\partial E_i}\right) = 0, \tag{6}$$

must be simultaneously satisfied for body force-free and charge-free ferroelectric materials.

A nonlinear multi-field coupling finite element method[44-48] is adopted here to solve those governing equations (4)-(6) numerically and simultaneously. With the principle of virtual work, we have the integral form of the governing equations,

$$\int_V \left\{ \frac{\partial f}{\partial \varepsilon_{ij}} \delta \varepsilon_{ij} + \frac{\partial f}{\partial E_i} \delta E_i + \frac{1}{L} \frac{\partial P_i}{\partial t} \delta P_i + \frac{\partial f}{\partial P_i} \delta P_i + \frac{\partial f}{\partial \xi_{ij}} \delta \xi_{ij} \right\} dV = \int_S \{ \tau_i \delta u_i - w \delta \phi + \pi_i \delta P_i \} dS \quad , \tag{7}$$

where $\xi_{ij} = P_{i,j}$, τ_i denote the surface traction, w denotes surface charge and $\frac{\partial f}{\partial P_{i,j}} n_j = \pi_i$ are the surface gradient flux, where n_j denote the components of normal unit vector of a surfaces. In the spatial discretization of finite element implementation, we used 8-node brick element with seven degrees of freedom at each node (three displacement components, one electrical potential and three polarization components). The Young's modulus along the crystal axis [001] direction of $Y_{[001]} = \frac{c_{11}^2 + c_{11}c_{12} - 2c_{12}^2}{c_{11} + c_{12}}$ was used to normalize applied compression stress σ_{33}. Table 1 lists all normalized parameters used in the present thermodynamic analysis and phase field simulations.

Fig. 2 is a schematic drawing of the studied $BaTiO_3$ nanoparticle, which top and bottom surfaces are covered by metal electrodes. The size of the nanoparticle is 10nm×10nm×10nm. To consider the material degradation at the electrode-ferroelectrics interface,[49-51] two degradation layers were sandwiched between the ferroelectrics and each of the electrodes at the upper and lower interfaces and the degradation layers were treated to be a dielectric material without any spontaneous polarization. Thus $\mathbf{P} = 0$ was used as the boundary condition along the two interfaces. For convenience, dimensionless material parameters with superscript * were used in the numerical calculations, while temperature and ATC were given in real physical dimensions in order to compare with the reported experimental results. The electrical open-circuit and mechanical traction-free boundary conditions were used on the lateral surfaces. Mechanical compression was applied on the top and bottom surfaces. The initial state of spontaneous polarization in the simulated

cell was achieved after the initial polarization evolution, during which a zero electric potential was applied across the two electrodes and a uniform random distribution of initial dimensionless polarizations with the maximum magnitude less than 0.005 triggered the polarization evolution with 50000 adaptive step increments. Then, an alternating electric voltage $\varphi^{ex,*} = \varphi_0^* \sin(2.5\pi\tau/125000)$ was applied across the electrodes, where τ was integer to denote the time step. Under each applied electric field at a given time step τ, the simulated ferroelectric nanoparticle was allowed to evolve once with a dimensionless time step of $\Delta t^* = 0.04$. The average polarization along the electric field direction was taken as the macroscopic response of the simulated system.

In the current work, the ATC ΔT was calculated with Eq. (1) and the heat capacity $C_E = 3.05\times10^6$ J/Km was assumed to be a constant, as did in the previous work.[11,12,51-54] The values of $P_3^*(T)$ were extracted from the upper right branch of P-E hysteresis loops with $E_3^* > 0$. The maximum normalized electric field E_3^*=1.5 corresponds to the electric field E_3= 144.752 kV/cm. Since external electric field and mechanical compression are both applied along x_3 direction and the simulated nanoparticle shown in Fig. 2 has the cubic crysttaline symmetry, polarizations P_1^* and P_2^* have the same possibility in the ferroelectric behavior. Thus, we can base on polarizations P_1^* and P_3^* to introduce four phases or polarization variants, which are *ab* phase ($P_1^* \neq 0$, P_3^*=0), *abc* phase ($P_1^* \neq 0$, $P_3^* \neq 0$), *c* phase (P_1^*=0, $P_3^* \neq 0$), and paraelectric phase ($P_1^* = P_3^* = 0$). Note that the *abc* phase is one phase, rather than a combination of the *ab* phase and the *c* phase, and $P_3^* \neq 0$ in the *abc* phase. Without any applied electric field, applying mechanical compression may let the *ab* phase occupy the lowest energy state. With the sutained compression, an applied electric field causes the *ab* phase to the *abc* phase and then the *c* phase transition. When

the applied electric field is unloaded from its maximum value to zero, the *ab* phase will recovered if no energy barriers are around the *c* or *abc* phase, while the *c* or *abc* phase will survive and give a finite value of remnant polarization, if energy barriers are there around the *c* or *abc* phase. In the current work, only survived phases at reduced-to-zero or reduced-to-one-specific electric field are of interest and obviously, the survived phases depend on the electric field loading history, the magnitude of the mechanical compression and temperature as well.

3. Results and Discussion

3.1 Thermodynmic analysis

Fig. 3 indicates the thermodynamic results based on Eq. (2) at different temperatures and external electric fields E_3^* under sustained mechanical compression of σ_{33}^*=-0.002, where polarization P_2^*=0, applied stress $\sigma_{11}^*=\sigma_{22}^*=\sigma_{12}^*=\sigma_{13}^*=\sigma_{23}^*=0$ and electric fields $E_1^*=E_2^*=0$. Fig. 3(A) shows the asymmetric three dimensional (3D) free energy landscape at temperature 323 K and E_3^*=0, indicating the possible ferroelectric *ab* phase, *abc* phase and *c* phase, and the paraelectric cubic (C) phase. As an example, the arrows in Fig. 3(A) illustrate the potential path with lowest resistance for the phase transition and the polarization rotation angle is determined based on the path. Fig. 3(B) shows the two possible polarization rotation paths from the *ab* phase to the *abc* phase, and then *c* phase at *T*=293 K with the increase of electric field, illustrating that two states of the *abc* phase ($P_1>0, P_3>0$ and $P_1<0, P_3>0$) may be induced by external electric field E_3^*. Figs. 3 (C)-(F) give the minimum free energy paths versus the rotation angle at various temperatures with respect to external electric fields of E_3^*=0, 0.2, 0.4 and 0.8, respectively. Fig. 3(C) shows that

without external electric field, the *ab* phase, at the rotation angle of 45°, dominates in the temperature range from 273 K to 403 K. Once an electric field is applied, polarizations in the *ab* phase will try to align themselves towards the direction of applied field, i.e., the x_3 direction, thereby changing the rotation angle. The rotation angle depends on the strength of the applied field and temperature as well. Once the polarizations in the original *ab* phase do not completely perpendicular to the x_3 direction, the original *ab* phase is changed to the *abc* phase. Fig. 3 (D) presents that the electric field E_3^*=0.2 induces two possible oriented *abc* phases at temperature 273 K. With the temperature increase, the Gibbs free energy of both phases is enhanced. At temperature 323 K, energy barrier appears around the *c* phase and the *c* phase becomes the survived phase. With temperature further increases to 373 K, however, the energy barrier disappears and the *c* phase becomes un-survived at temperature 373 K. From 373 K to 403 K, the *abc* phase dominates and increases continuously its free energy with the temperature increase. When the external electric field increases to E_3^*=0.4, as shown in Fig. 3(E), the energy barriers around the *c* phase appears at temperature 303 K with a lower free energy than that shown in Fig. 3(D) under E_3^*=0.2 and at temperature 323 K. When temperature increases to 403 K, the *c* phase becomes un-survived due to the disappearing of the energy barrier around it. Note the critical temperature for the onset of the survived *c* phase under E_3^*=0.4, 303 K, is lower than that of 323 K under E_3^*=0.2 shown in Fig. 3(D), while the end temperature of the survived *c* phase, 403 K, is higher than that of 373 K under E_3^*=0.2. Under a sustained mechanical compression, varying the strength of applied electric field changes the onset and end temperatures of the survived *c* phase, as shown in Fig. 3 (F) for E_3^*=0.8, where the onset and end temperatures are 283 K and higher than 403 K, respectively. The transition between survived *c* phase and survived *abc* phase is simply called the transition between the *c* and

abc phases in the present work, which are also accompanied by large isothermal entropy change, analogy to the ultrahigh isothermal entropy change during the transition between the *ab* phase and the *c* phase.[37,38] Two types electric-field-induced-pseudo-phase transition (EFIPPT) are defined based on the phase transition between the *abc* phase and the *c* phase. As temperature increases, the phase transition from the *abc* phase to the *c* phase, called type-II EFIPPT, occurs first, during which macroscopic polarization along the direction of applied electric field jumps from a finite nonzero value to another higher value; whereas the inverse phase transition from the *c* phase to the *abc* phase, named type-I EFIPPT, occurs at a higher temperature.

3.2. Phase field simulation results

The phase field simulations results are shown and compared with the thermodynamic analysis in this section. Figs. 4(A)-(F) show the averaged polarization $\left\langle P_3^* \right\rangle \sim E_3^*$ hysteresis loops of the ferroelectric nanoparticle under mechanical compressions of σ_{33}^*=0, -0.001, -0.0015, -0.00175, -0.002 and -0.00218, respectively. Without any mechanical compression, both remnant polarization and coercive field decrease monotonously with the temperature increase, as shown in Fig. 4(A). When the temperature increases to its Curie temperature 379 K, double-hysteresis loop, which originates from typical electric-field-induced phase transition from paraelectric phase to ferroelectric phase, appears and the remnant polarization is 0.014. When the mechanical compression increases to $\sigma_{33}^* = -0.001$, as shown in Fig. 4(B), the remnant polarization and coercive field decrease with the increase of temperature from 273 K to 348 K. At temperature 348 K, double-hysteresis loop shows up and the remnant polarization is 0.452. Increasing temperature from

348 K continuously shrinks the $\langle P_3^* \rangle \sim E_3^*$ double-hysteresis loop to a nonlinear curve passing through the origin with a zero remnant polarization and a zero coercive field at temperature 398K. Fig. 4(C) shows the $\langle P_3^* \rangle \sim E_3^*$ hysteresis loops under compression $\sigma_{33}^* = -0.0015$. The shapes of $\langle P_3^* \rangle \sim E_3^*$ loops at temperatures of 298 K and 333 K are abnormal with regard to the polarization axis, looking like between the normal $\langle P_3^* \rangle \sim E_3^*$ curve shape shown in Fig. 4(A) and the double-hysteresis loop shape. When the temperature reaches to 348 K, the $\langle P_3^* \rangle \sim E_3^*$ curve is completely confined in the first coordinator quarter of $\langle P_3^* \rangle > 0$ and $E_3^* > 0$, as double-hysteresis loop shows up. Then, increasing temperature shrinks the double-hysteresis loops until temperature 398 K, at which a nonlinear $\langle P_3^* \rangle \sim E_3^*$ curve appears. The similar behavior to that in Fig. 4(C) was observed under compression σ_{33}^*=-0.00175 as shown in Fig. 4(D), except that the shapes of $\langle P_3^* \rangle \sim E_3^*$ loops at temperatures of 298 K and 323 K become more abnormal with respect to the polarization axis. This implies that increasing the magnitude of mechanical compression might promote the appearance of double-hysteresis loops, and this hypothesis is verified by the phase field simulations. Figs. 4(E)-(F) show $\langle P_3^* \rangle \sim E_3^*$ loops under mechanical compression σ_{33}^*=-0.002 and -0.00218, respectively, indicating that the double-hysteresis loops dominate the response of polarization versus external electric field over the temperature range from 298 K to 373 K except of a nonlinear $\langle P_3^* \rangle \sim E_3^*$ curve at 398 K.

Figs. 5(A)-(F) show the averaged polarization $\langle P_3^* \rangle$ versus temperature under each of electric fields and different sustained mechanical compressions. Without any applied compression, the averaged polarization under each external electric field monotonically decreases with the increase of temperature, as shown in Fig. 5(A). In this case, the remnant polarization, i.e., the averaged

polarization $\langle P_3^* \rangle$ at E_3^*=0 drops sharply from a finite value to zero at temperature 379 K, which is defined as the type-I PFOPT in the previous work.[37] When the applied field have a finite nonzero value, the averaged polarization $\langle P_3^* \rangle$ versus temperature T exhibits the electric field induced polarization behavior. Increasing the magnitude of compression to σ_{33}^* =-0.001 lowers the type-I PFOPT temperature to 351 K, as shown in Fig. 5(B). Further increasing the magnitude of compression to σ_{33}^* =-0.0015 not only further reduces the type-I PFOPT temperature to 337 K, but induces the type-II PFOPT, as shown in Fig. 5(C), where the remnant polarization, i.e., the averaged polarization $\langle P_3^* \rangle$ at E_3^*=0 jumps sharply from zero to a finite value at temperature 283 K. More significantly, Fig. 5(C) also shows a completely new phenomenon regarding to electric field induced polarization. For instance, when temperature increases from 273 K to 277 K, the averaged polarization $\langle P_3^* \rangle$ at a sustained applied field of E_3^*=0.1, decreases slightly from 0.114 to 0.112 , and around temperature T= 279 K, the averaged polarization suddenly jumps from 0.112 to 0.88, as shown in Fig. 5(C), which is called the type-II EFIPPT, as described above. After the type-II EFIPPT temperature, increasing temperature from 279 K to 345 K makes the averaged polarization shrinks from 0.88 to 0.251, and around temperature T=347 K, the averaged polarization suddenly falls from 0.251 to 0.0976, as shown in Fig. 5(C), which is named the type-I EFIPPT. It should be noted that both polarization abrupt rise and deep fall in type-I and type-II EFIPPTs are not so steeply as those in type-I and type-II PFOPTs, in particular, type-I EFIPPT will evolve to the electric field induced polarization at higher applied electric field by gradually losing the deep falling. Like type-I and type-II PIOPTs, type-I and type-II EFIPPTs also play important roles in negative and positive ECEs, which will be discussed later. Fig. 5(D) shows that under sustained σ_{33}^* =-0.00175, the behavior of the averaged polarization $\langle P_3^* \rangle$ versus temperature T is very much

similar to that under σ_{33}^{*}=-0.0015 shown in Fig. 5 (C), except that the difference between the two types PFOPT temperatures shrinks from 46 K to 32 K and the according decrease in the difference between the two types EFIPPT temperatures. When the compression increases to σ_{33}^{*} =-0.002, shown in Fig. 5(E), the remnant polarization maintains zero over the studied temperature range, meaning that the PFOPT disappears once the sustained compression exceeds σ_{33}^{*} =-0.002. However, when a specific external electric field is applied, the two types of EFIPPT will take place. In this case, only EFIPPTs cause the negative and positive ECEs. Further increasing the magnitude of compression increases the threshold of electric field for the appearance of EFIPPT. For example, under σ_{33}^{*} = -0.00218, no EFIPPTs occur at the electric field E_3^{*}=0.1 at all, and EFIPPTs start to appear at E_3^{*}=0.2.

Fig. 6(A) shows the temperature-compression phase diagrams of the simulated $BaTiO_3$ nanoparticle based on the remnant polarization. Under low compression from zero to σ_{33}^{*}=-0.005, the Curie temperature decreases with the increase of mechanical compression. When the mechanical compression further increases to σ_{33}^{*}=-0.0075, the type-I PFOPT appears in addition to FOPFT and both are associated with ultrahigh positive EC effect. The type-I PFOPT temperature decreases sharply with the increase of compression magnitude, while the Curie temperature increases. When the magnitude of compression is increased to the range from σ_{33}^{*}=-0.0015 to σ_{33}^{*}=-0.00175, the type-II PFOPT occurs at temperatures lower than the corresponding type-I PFOPT temperatures. The wine dotted line shows the results of the same nanoparticle without the degradation layers.[38] It is obvious that the combination of mechanical compression and electrical depolarization reduces the Curie temperature and the PFOPT temperature, implying that the electrical depolarization by

degradation layers plays a certain role here. As reported in the previous work,[37,38] the type-II PFOPT is induced only by the mechanical compression, while the type-I PFOPT can be caused by mechanical compression or/and electrical depolarization. Fig. 6(B) presents the domain structures of the studied nanoparticle at the mechanical compression $\sigma_{33}^{*} = -0.00175$ with respect to different temperatures, every ten degrees are chosen corresponding to the points shown in Fig. 6(A). When the temperature increases from 273 K to 295 K, the *ab* phase dominates. Once the temperature increases to 297 K, the *c* phase appears and predominates until temperature 325 K. Once the temperature increases to 327 K, the *ab* phase appears again. The transition from the *ab* phase to the *c* phase (or from the *c* phase to the *ab* phase) is accompanied with a large decrease (or increase) in the isothermal entropy of the studied nanoparticle, which is the thermodynamic mechanism of the ultrahigh positive/negative EC effects.

When the mechanical compression is large enough, i.e., higher than σ_{33}^{*}=-0.002 in the current work, the ferroelectric domain configuration cross the studied temperature range is basically controlled by the in-plane *ab* phase, which gives electric field induced double-hysteresis loops and zero remnant polarization, as shown in Figs. 4(E)-(F). The PFOPTs no longer exist in this circumstance. When electric field is applied to the nanoparticle under such a sustained high compression, EFIPPTs will take place between the *abc* phase and the *c* phase. Fig. 7(A) presents the temperature-external electric field phase diagram of the simulated $BaTiO_3$ nanoparticle under sustained mechanical compression σ_{33}^{*}=-0.002, where E_3^{*}=0.1 is the threshold of applied electric field to induce EFIPPTs. With the increase in electric field from E_3^{*}=0.1, the polarization in the *abc* phase rotates toward to the *c* phase until E_3^{*}=0.8, at and beyond which the *abc* phase disappears

completely and replaced by the *c* phase. Besides, increasing the applied electric field raises the ferroelectric/paraelectric phase transition temperature. Fig. 7(B) gives the domain structures under the applied mechanical compression $\sigma_{33}^{*} = -0.002$ and applied electric field E_3^{*}=0.2 with respect to different temperatures, every ten degrees are chosen corresponding to the points shown in Fig. 7(A). When the temperature increases to and beyond 297 K, the *abc* phase will be replaced by the *c* phase until temperature 325 K, at which the *abc* phase appears again as the result of energy minimization and loading history. With the further increase in temperature, the polarization in the *abc* phase will continue to rotate, and finally at temperature 393 K, the *abc* phase vanishes and the *c* phase emerges. Comparing Fig. 6 and Fig. 7 with Fig. 3 indicates that the phase field simulation results of electric field induced phase transitions are consistent with the thermodynamic analysis.

Figs. 8(A)-(F) give the ATC ΔT as a function of temperature under mechanical compressions of σ_{33}^{*} = 0, -0.001, -0.0015, -0.00175, -0.002, -0.00218, respectively. Without any applied compression, as shown in Fig. 8(A), all ATC ΔT peaks occur at temperature 377 K, independent of the variation strength of applied electric field. This is because the PFOPT temperature is independent of external electric field, as the Curie temperature. As expected, the peak gets higher with the increase of ΔE_3^{*} and the maximum ATC is ΔT=3.596 K with the highest applied electric field ΔE_3^{*}=1.5. Under the sustained compression of σ_{33}^{*}= -0.001, all ATC ΔT peaks are located at temperature 350 K, as shown in Fig. 8(B). Comparing Fig. 5(B) to Fig. 5(A) indicates that the mechanical compression of σ_{33}^{*}= -0.001 makes the type-I PFOPT temperature 26 K lower than that without any applied compression. The ATC peak temperature under σ_{33}^{*}= -0.001 is 27 K lower in comparison with that without any applied compression. The slightly difference between them is

attributed to the slightly difference between the PFOPT temperature and the peak temperature of ATC ΔT in the numerical calculation. Nevertheless, both Fig. 8(A) and 8(B) illustrate that the ATC ΔT peak temperature is close to the type-I PFOPT temperature. Fig. 8(C) shows that both positive and negative ultrahigh EC effects take place under the applied mechanical compression of σ_{33}^{*}=-0.0015. All positive ATC ΔT peaks are located at temperature 336 K, which is near the type-I PFOPT temperature 337 K under σ_{33}^{*}=-0.0015, as shown in Fig. 5(C). The negative ATC ΔT, however, shows three valleys (called peaks also for simplification) at 277 K, 279 K and 280 K, which are respectively 59 K, 57 K and 56 K lower than the positive ATC ΔT peak. Checking Fig. 5(C) carefully, one will find that the type-II EFIPPTs at E_3^{*}=0.1 and E_3^{*}=0.2 are very similar as type-II PFOPTs except of the polarization jump from a low value to a large value. The type-II EFIPPT temperatures are almost coincided with the negative ATC ΔT peak temperatures. This indicates that a polarization jump will induce a negative ATC ΔT peak. As a direct consequence, a polarization drop will induce a positive ATC ΔT peak. Due to the type-I EFIPPTs, the positive ATC ΔT peaks become diffuse, as shown in Fig. 8(C). Fig. 8(D) shows the behavior of the ATC ΔT versus temperature under mechanical compression of σ_{33}^{*}=-0.00175, indicating that the peaks of negative/positive ATC ΔT at ΔE_3^{*}=0.1, 0.2, and 0.3 appear at temperatures of 289 K/329 K, 285 K/335 K and 281 K/335 K, respectively. These temperatures are closely related to the type-II/I EFIPPT temperatures shown in Fig. 5(D). In Fig. 8(D), the smallest temperature gap is 30 K between the negative and position peak temperatures. When the applied mechanical compression σ_{33}^{*} increases to -0.002, the peaks of negative/positive ATC ΔT at ΔE_3^{*}=0.1, 0.2, 0.3, and 0.6 appear at temperatures of 307 K/321 K, 297 K/331 K, 291 K/337 K, and 289 K/337 K, respectively, as shown in Fig. 8(E). These peaks are well separated from one another under the sustained

compression of σ_{33}^{*} =-0.002. The interesting finding is that the peaks of negative/positive ATC ΔT are around room temperature and the smallest temperature gap is 14 K, which are the ideal EC properties for real applications. Further increasing the compression to σ_{33}^{*} =-0.00218 reduces the smallest temperature gap to 10 K, as shown in Fig. 8(F), while the other features of the ATC ΔT versus temperature remain almost the same as these under σ_{33}^{*} =-0.002, which are also similar to the EC effect reported in antiferroelectric materials.[26,34,35] Comparing Figs. 8(C)-(F) with Figs. 8(A)-(B) indicates two significant features. One is the coexistence of negative/positive EC effects, which allows one to fully take the advantage during the cycling of an applied electric field. The other is the ATC ΔT peak temperature can be tuned by external electric field, especially when the external electric field is low, which allows one to optimize the operating temperature range. Thereby, double hysteresis loops associated with the coexistence of positive and negative EC effects in one tetragonal ferroelectric material will pave a completed new way for the material application in solid cooling devices.

The another potential application of the novel findings in the present work might be related to the pyroelectric effect, which is an inverse process of the electrocaloric effect, meaning that electricity will be generated by a change in temperature of a ferroelectric material. Thus, the pyroelectric effect might be significant near the PFOPT and EFIPPT temperatures, which will be investigated soon. Besides, large and electric field-tunable superelastic strains up to 0.85% has been realized[55,56] in a specially poled $BaTiO_3$ crystal cube via compression loading/unloading with a positive dc bias electric field along the poling direction, which mechanism is speculated to relate the PFOPT and EFIPPT.

4. Concluding remarks

In summary, phase field simulations, which take the combined contributions of electrical depolarization by degradation layers and mechanical compression, together with thermodynamic analysis were conducted to explore the underlying mechanism of double hysteresis loops and large negative and positive EC effects in tetragonal ferroelectric nanoparticles. The results suggest that the mechanism is attributed to two types of PFOPTs and two types of EFIPPTs. When the sustained mechanical compression is above a critical value, the mechanical compression may result in only the in-pane *ab* phase with zero averaged remnant polarization $\left\langle P_3^* \right\rangle$ along x_3 direction. Then, an applied electric field may cause the phase transition from the *abc* phase to the *c* phase. In this case, double-hysteresis loops may occur as the macro-response of polarization versus electric field below its ferroelectric Curie temperature and the negative/positive EC effects coexist in one tetragonal ferroelectric material. The maximum positive and negative values in adiabatic temperature change (ATC ΔT) shift with the magnitude of applied electric field change and depend on the compression magnitude. As temperature increases from 273 K, type-II EFIPPT occurs first, where the *abc* phase transits to the *c* phase, and then type-I EFIPPT happens by the inverse transition from the *c* phase to the *abc* phase. All those findings provide a deep understanding of the double hysteresis loops with the coexistence of positive and negative EC effects in one tetragonal ferroelectric material and open a new window for the application of ferroelectric materials in solid cooling devices.

Acknowledgement

The authors acknowledge the financial support from the Hong Kong Research Grants Council

under the General Research Fund, 622813.

References

1 M. E. Lines and A. M. Glass, P*rinciples and applications of ferroelectrics and related materials*, Oxford University Press, Clarendon, 1977.

2 J. D. Childress, *J. Appl. Phys.*, 1962, **33**, 1793.

3 G. G. Wiseman and J. K. Kuebler, *Phys. Rev.*, 1963, **131**, 2023.

4 P. D. Thacher, *J. Appl. Phys.*, 1968, **39**, 1996.

5 B. Rožič, B. Malič, H. Urš ič, J. Holc, M. Kosec, B. Neese, Q. M. Zhang and Z. Kutnjak, *Ferroelectrics*, 2010, **405**, 26-31.

6 S. G. Lu and Q. M. Zhang. *Adv. Mater.*, 2009, **21**, 1983-1987.

7 Y. S. Ju, *J. Electron. Packag.*, 2010, **132**, 041004.

8 L. Liu, Y. Liu, B. Li and J. Leng, *Appl. Phys. Lett.*, 2011, **99**, 181908.

9 M. Valant, *Prog. Mater. Sci.*, 2012, **57**, 980-1009.

10 R. Radebaugh, W. N. Lawless, J. D. Siegwarth and A. J. Morrow. *Cryogenics*, 1979, **19**, 187-208.

11 A. S. Mischenko, Q. Zhang, J. F. Scott, R. W. Whatmore and N. D. Mathur, *Science*, 2006, **311**, 1270-1271.

12 B. Neese, B. Chu, S. G. Lu, Y. Wang, E. Furman and Q. M. Zhang, *Science*, 2008, **321**, 821-823.

13 A. S. Mischenko, Q. Zhang, R. W. Whatmore, J. F. Scott and N. D. Mathur, *Appl. Phys. Lett.*, 2006, **89**, 242912.

14 B. Neese, S. G. Lu, B. Chu and Q. M. Zhang, *Appl. Phys. Lett.*, 2009, **94**, 042910.

15 H. Chen, T. L. Ren, X. M. Wu, Y. Yang and L. T. Liu, *Appl. Phys. Lett.*, 2009, **94**, 182902.

16 J. Hagberg, A. Uusimaki and H. Jantunen, *Appl. Phys. Lett.*, 2008, **92**, 132909.

17 S. G. Lu, B. Rožič, Q. M. Zhang, Z. Kutnjak and B. Neese, *Appl. Phys. Lett.*, 2011, **98**, 122906.

18 T. M. Correia, J. S. Young, R. W. Whatmore, J. F. Scott, N. D. Mathur and Q. Zhang, *Appl. Phys. Lett.*, 2009, **95**, 182904.

19 Y. Bai, X. Han, X.-C. Zheng and L. J. Qiao, *Sci. Rep.*, 2013, **3**, 2895.

20 T. Nishimatsu, J. A. Barr and S. P. Beckman, *J. Phys. Soc. Jpn.*, 2013, **82**, 114605.

21 J. Wang, M. Liu, Y. Zhang, T. Shimada, S. Shi and T. Kitamura, *J. Appl. Phys.*, 2014, **115**, 164102.

22 B. Li, W. J. Ren, X. W. Wang, H. Meng, X. G. Liu, Z. J. Wang and Z. D. Zhang, *Appl. Phys. Lett.*, 2010, **96**, 102903.

23 B. Asbani, J.-L. Dellis, A. Lahmar, M. Courty, M. Amjoud, Y. Gagou, K. Djellab, D. Mezzane, Z. Kutnjak and M. El Marssi, *Appl. Phys. Lett.*, 2015, **106**, 042902.

24 X. Moya , E. Stern-Taulats, S. Crossley, D. González-Alonso, S. Kar-Narayan, A. Planes, L. Mañosa and N. D. Mathur, *Adv. Mater.*, 2013, **25**, 1360-136

25 J. Peräntie, J. Hagberg, A. Uusimäki and H. Jantunen, *Phys. Rev. B*, 2010, **82**, 134119.

26 Y. Bai, G. P. Zheng and S. Q. Shi, *Mater. Res. Bull.*, 2011, **46**, 1866.

27 I. Ponomareva and S. Lisenkov. *Phys. Rev. Lett.*, 2012, **108**, 167604.

28 F. L. Goupil, A. Berenov, A.-K. Axelsson, M. Valant and N. M. Alford, *J. Appl. Phys.*, 2012, **111**, 124109.

29 L. Luo, M. Dietze, C.-H. Solterbeck, M. Es-Souni and H. Luo, *Appl. Phys. Lett.*, 2012, **101**, 062907.

30 J. Peräntie, J. Hagberg, A. Uusimäki, J. Tian and P. Han, *J. Appl. Phys.*, 2012, **112**, 034117.

31 S. Uddin, G.-P. Zheng, Y. Iqbal, R. Ubic and J. Yang, *J. Appl. Phys.*, 2013, **114**, 213519.

32 X. Jiang, L. Luo, B. Wang, W. Li and H. Chen, *Ceram. Int.*, 2014, **40**, 2627-2634.

33 A. K. Axelsson, F. Le Goupil, L. J. Dunne, G. Manos, M. Valant and N. McN. Alford, *Appl. Phys. Lett.*, 2013, **102**, 102902.

34 R. Pirc, B. Rožič, J. Koruza, B. Malič and Z. Kutnjak, *EPL*, 2014, **107**, 17002

35 W. Geng, Y. Liu, X. Meng, L. Bellaiche, J. F. Scott, B. Dkhil and A. Jiang. *Adv. Mater.*, 2015, DOI: 10.1002/adma.201501100

36 I. Bhaumik, S. Ganesamoorthy, R. Bhatt, A. K. Karnal, P. K. Gupta, S. Takekawa and K. Kitamura. *EPL*, 2014, **107**, 47001.

37 H. H. Wu, J. Zhu and T. Y. Zhang, *RSC Adv.*, 2015, **5**, 37476-37484

38 H. H. Wu, J. Zhu and T. Y. Zhang, Nano energy, accepted.

39 M. J. Haun, E. Furman, S. J. Jang, H. A. McKinstry and L. E. Cross, *J. Appl. Phys.*, 1987, **62**, 3331.

40 N. A. Pertsev, A. G. Zembilgotov and A. K. Tagantsev, *Phys. Rev. Lett.*, 1998, **80**, 1988.

41 Y. L. Li, L. E. Cross and L. Q. Chen, *J. Appl. Phys.*, 2005, **98**, 064101.

42 H. H. Wu, J. Wang, S. G. Cao, L. Q. Chen and T. Y. Zhang, *J. Appl. Phys.*, 2013, **114**, 164108.

43 H. H. Wu, J. Wang, S. G. Cao, L. Q. Chen and T. Y. Zhang, *Smart Mater. Struct.*, 2014, **23**, 025004.

44 M. Kamlah, A. Liskowsky, R. McMeeking and H. Balke, Int. J. Solids Struct., 2005, **42**, 2949-64.

45 D. Schrade, R. Mueller, B. Xu and D. Gross, *Comput. Methods Appl. Mech. Eng.*, 2007, **196**, 4365-74.

46 Y. Su and C. M. Landis, *J. Mech. Phys. Solids*, 2007, **55**, 280-305.

47 J. Wang and M. Kamlah, *Smart Mater. Struct.*, 2009, **18**, 104008.

48 L. Jiang, Y. Zhou, Y. Zhang, Q. Yang, Y. Gu and L. Q. Chen, *Acta Mater.*, 2015, **90**, 344-354.

49 A. Artemev, *Philos. Mag.*, 2010, **90**, 89-101.

50 X. L. Li, B. Chen, H. Y. Jing, H. B. Lu, B. R. Zhao, Z. H. Mai and Q. J. Jia, *Appl. Phys. Lett.*, 2005, **87**, 222905.

51 M. Liu and J. Wang, *Sci. Rep.*, 2015, **5**, 7728.

53 J. Karthik and L. W. Martina, *Appl. Phys. Lett.*, 2011, **99**, 032904.

54 G. Akcay, S. P. Alpay, J. V. Mantese and G. A. Rossetti, *Appl. Phys. Lett.*, 2007, **90**, 252909.

55 E. Burcsu, G. Ravichandran and K. Bhattacharya, *Appl. Phys. Lett.*, 2000, **77**, 1698.

56 Y. W. Li, X. B. Ren, F. X. Li, H. S. Luo and D. N. Fang, *Appl. Phys. Lett.*, 2013, **102**, 092905.

Table 1. Values of the normalized coefficients used in the calculation

$\alpha_{11}^{\oplus *}$	α_{11}^{*}	$\alpha_{12}^{\oplus *}$	α_{12}^{*}	α_{111}^{*}	α_{112}^{*}	α_{123}^{*}	α_{1111}^{*}
-0.38193	0.62287	1.4523	1.1670	0.15932	-0.24009	-0.30791	0.32152
α_{1112}^{*}	α_{1122}^{*}	α_{1123}^{*}	q_{11}^{*}	q_{12}^{*}	q_{44}^{*}	Q_{11}^{*}	Q_{12}^{*}
0.21049	0.13625	0.11378	302.96	8.3630	190.65	0.00676	-0.0022984
Q_{44}^{*}	c_{11}^{*}	c_{12}^{*}	c_{44}^{*}	G_{11}^{*}	G_{12}^{*}	G_{44}^{*}	$G_{44}^{'*}$
0.0019604	70943	38421	48624	0.6	0	0.3	0.3

Note: The Voigt notation of q_{ijkl}, Q_{ijkl}, c_{ijkl} and G_{ijkl} are used here.

Figure captions

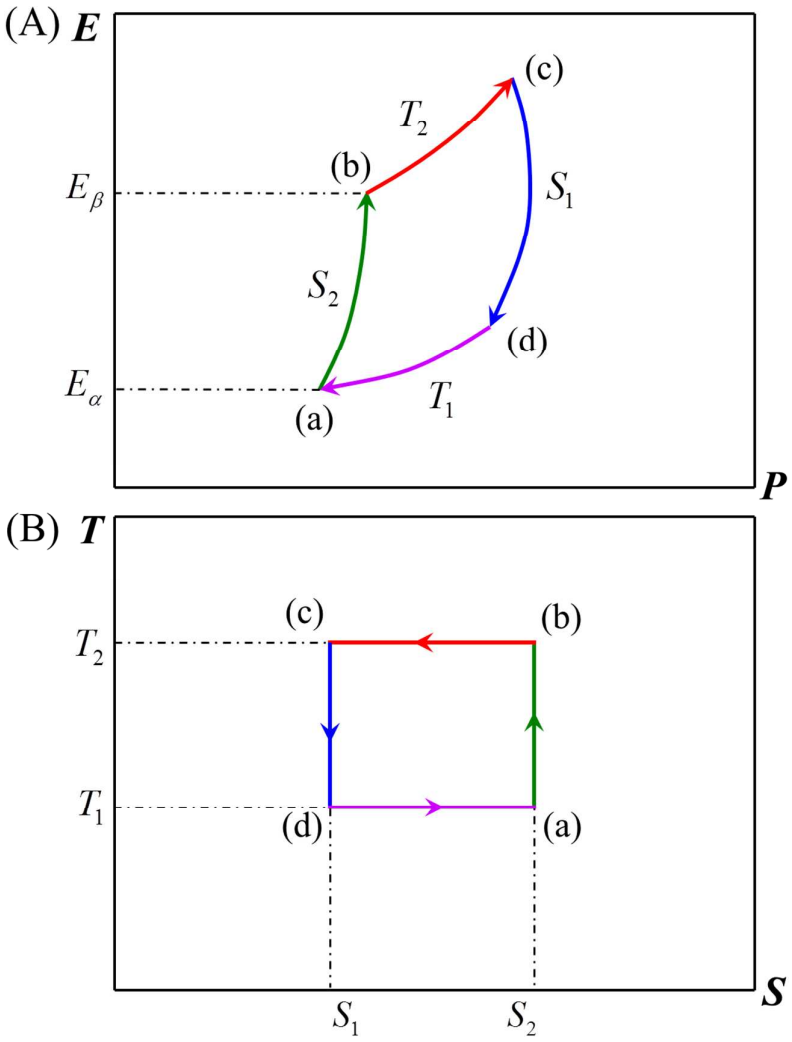

Fig. 1 The conventional thermodynamic cycle of EC materials involving two isothermal changes and two isentropic temperature changes for a positive EC refrigeration. (A) *E*-*P* diagram, (B) *T*-*S* diagram.

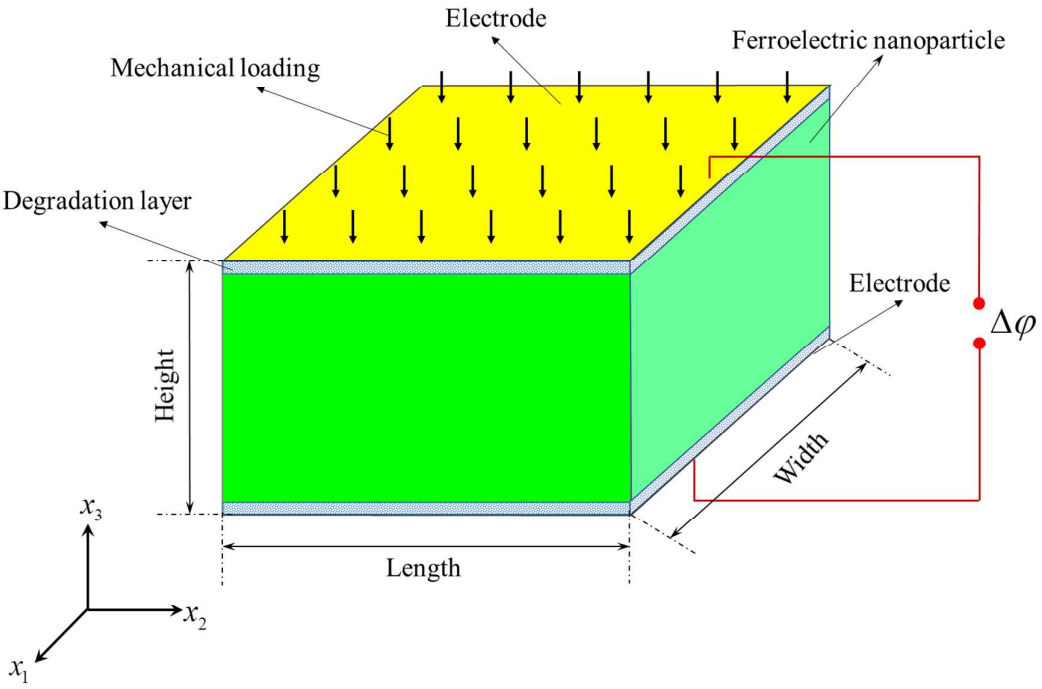

Fig. 2 Schematic drawing of a ferroelectric nanoparticle with degradation layers sandwiched between electrodes and ferroelectrics under a mechanical compression along the x_3 direction.

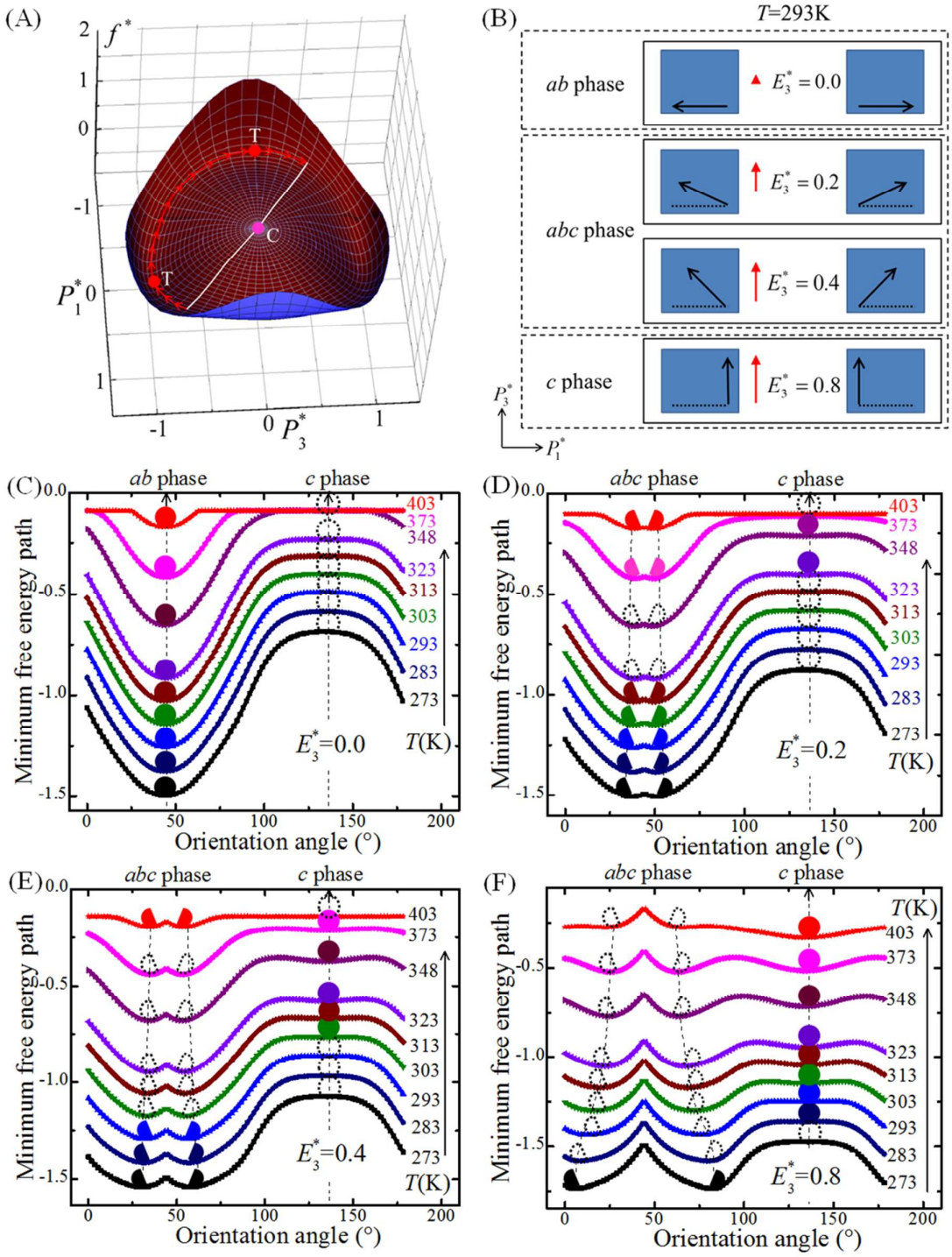

Fig. 3 The thermodynamic free energy with respect to different temperatures under sustained mechanical compression of $\sigma_{33}^* = -0.002$, where $P_2^*=0$, $\sigma_{11}^*=\sigma_{22}^*=\sigma_{12}^*=\sigma_{13}^*=\sigma_{23}^*=0$ and $E_1^*=E_2^*=0$: (A) The three dimensional free energy landscape at temperature 323K; (B) The initial *ab* phase,

electric field-induced *abc* phase and *c* phase at the temperature 293 K; (C)-(F) The minimum free energy paths along the orientation angle with respect to different electric fields of E_3^*=0, 0.2, 0.4 and 0.8, respectively, as indicated by the arrows in (A). The abbreviation T and C represent tetragonal and cubic phase, respectively. Symbols of solid and open balls indicate the positions of the *ab* and *c* phases and symbols of solid and open half balls mark the positions of the *abc* phase, where solid and open denote the phases will be survived and not survived, respectively, after the applied field decreases from its maximum value to zero. The *abc* phase has two possible states, as indicated in (B).

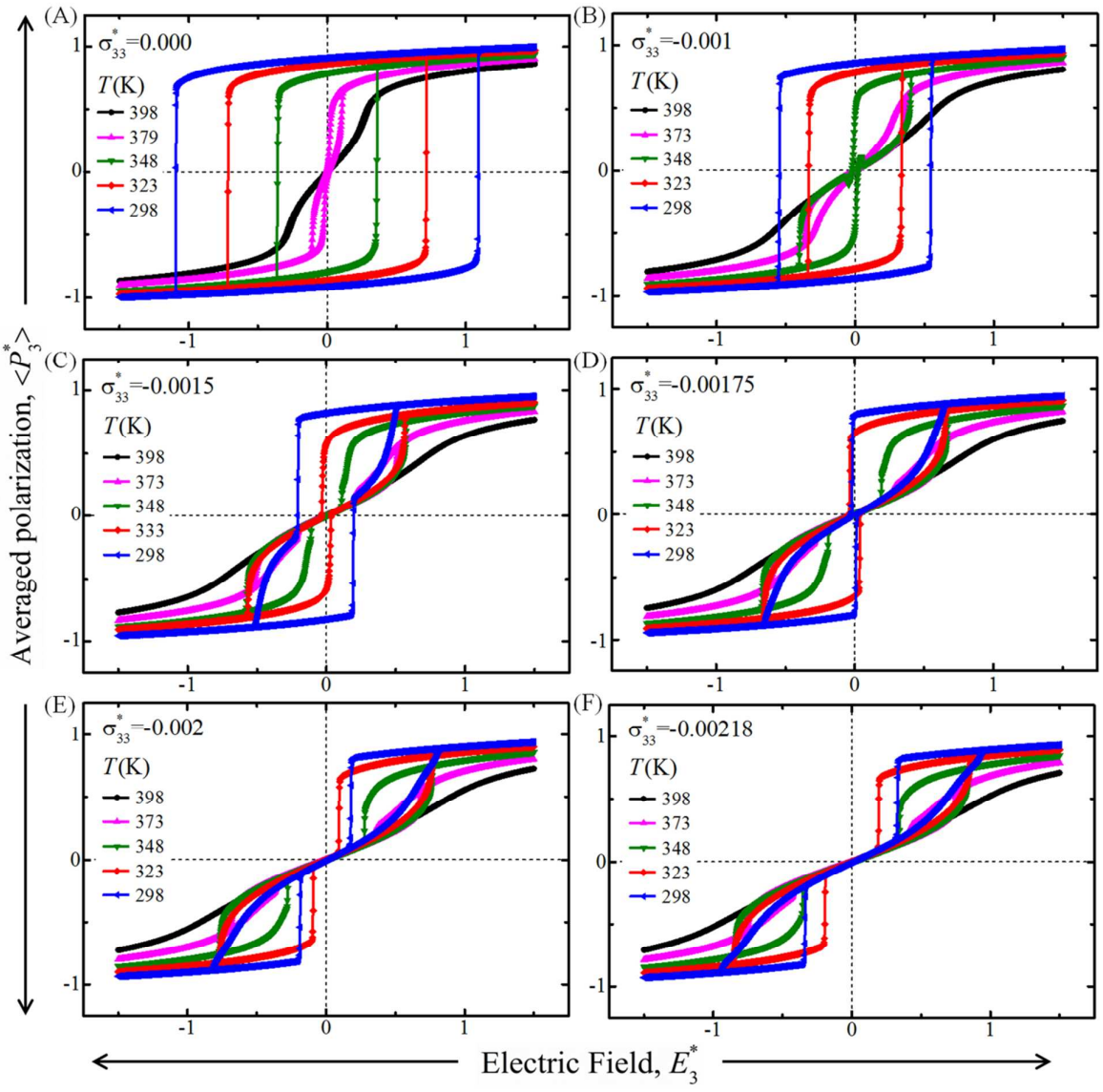

Fig. 4 Hysteresis loops of the $BaTiO_3$ nanoparticles under mechanical compression (A) σ_{33}^*=0, (B) σ_{33}^*=-0.001, (C) σ_{33}^*=-0.0015, (D) σ_{33}^*=-0.00175, (E) σ_{33}^*=-0.002, (F) σ_{33}^*=-0.00218.

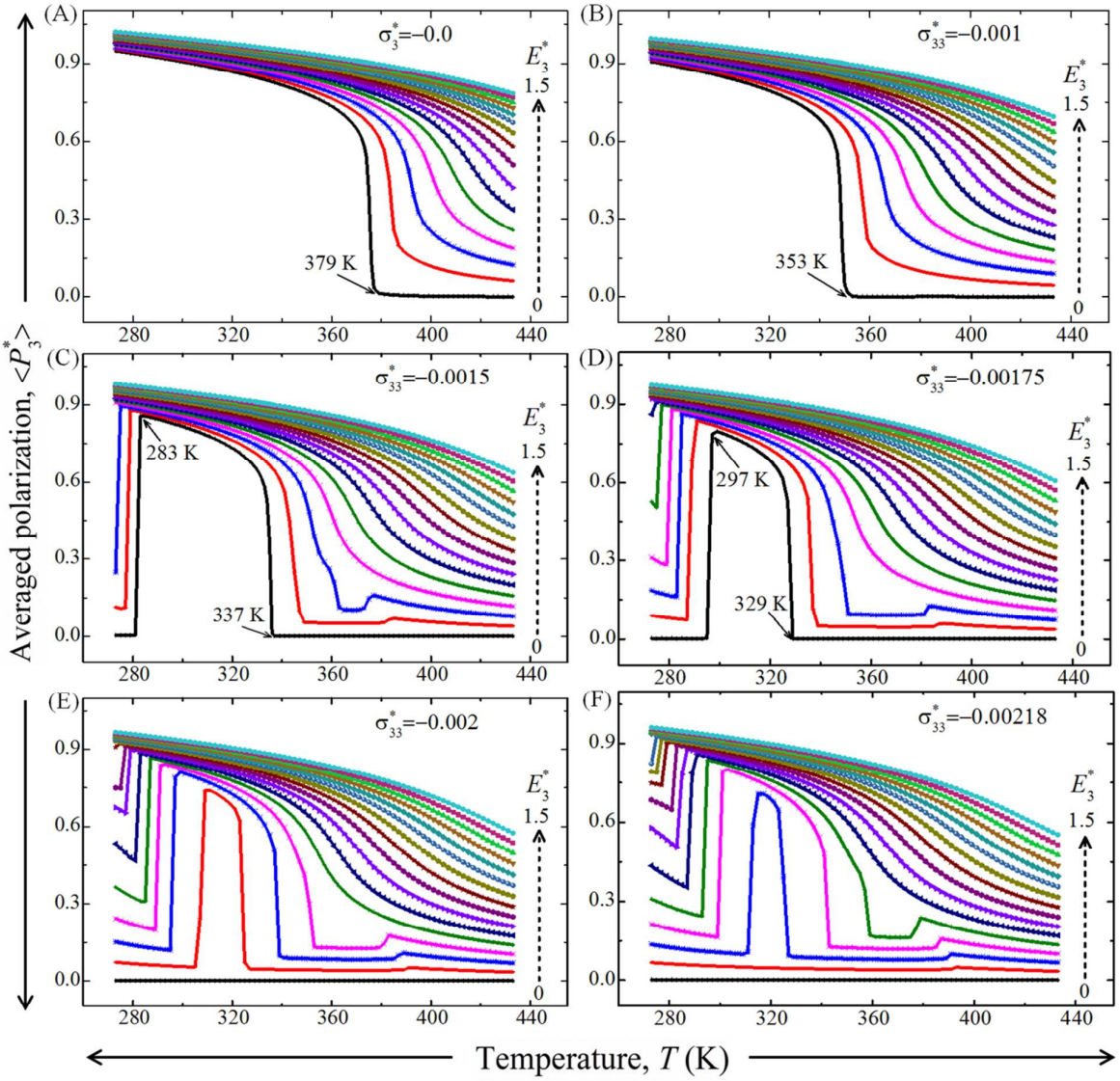

Fig. 5 Averaged polarization $\left\langle P_3^* \right\rangle$ versus temperature curves under sustained mechanical compression (A) σ_{33}^*=0, (B) σ_{33}^*=-0.001, (C) σ_{33}^*=-0.0015, (D) σ_{33}^*=-0.00175, (E) σ_{33}^*=-0.002, (F) σ_{33}^*=-0.00218.

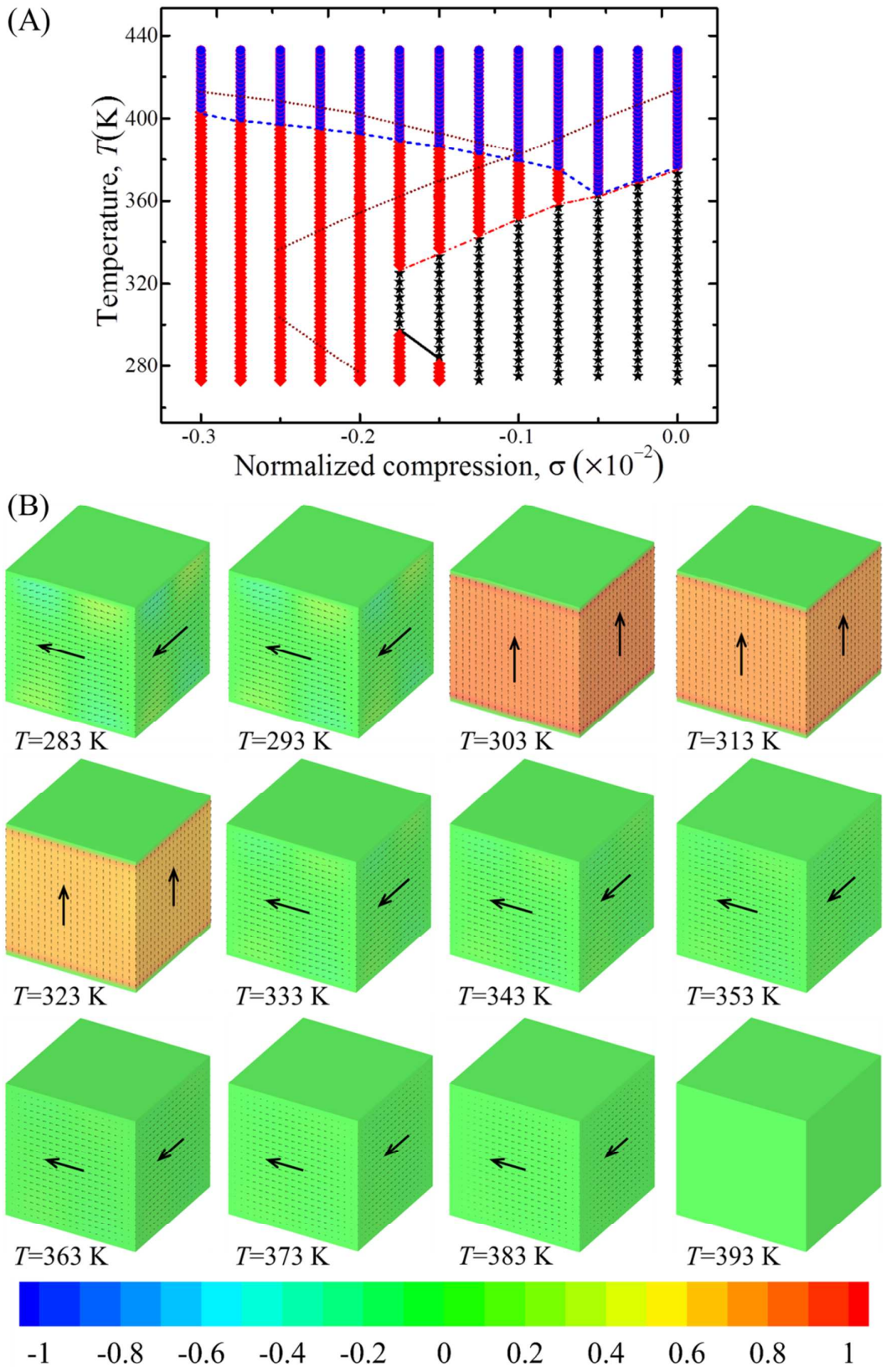

Fig. 6 (A) Temperature-compression phase diagram of the $BaTiO_3$ nanoparticles based on the

remnant polarization. Symbols: ★ *c* phase, ◆ *ab* phase, ● paraelectric phase; (B) Domain structures of the nanoparticles corresponding to the remnant polarizations, where the applied electric field is reduced from E_3^*=1.5 to zero, at the mechanical compression σ_{33}^*=-0.00175 with respect to different temperatures, every ten degrees are chosen corresponds to the points shown in (A).

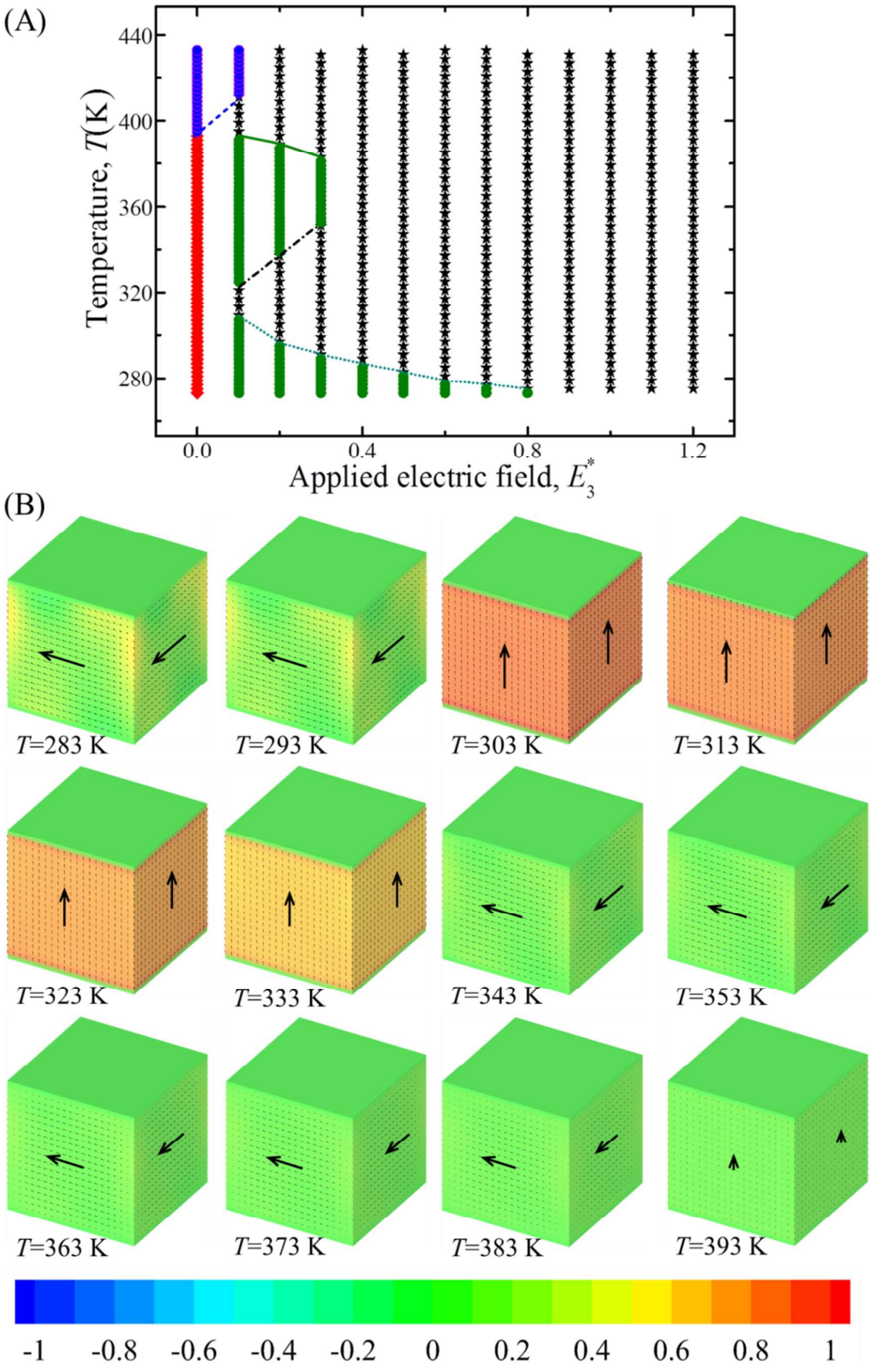

Fig. 7 (A) Temperature-electric field phase diagram of the $BaTiO_3$ nanoparticles under sustained

compression $\sigma_{33}^{*} = -0.002$, where the applied electric field is reduced from E_3^{*}=1.5 to a specific value. Symbols: ★ *c* phase, ◆ *ab* phase, ● paraelectric phase, ● *abc* phase. (B) Domain structures under sustained compression $\sigma_{33}^{*} = -0.002$ and applied electric field E_3^{*}=0.2 at temperatures ranging from 283K to 393K.

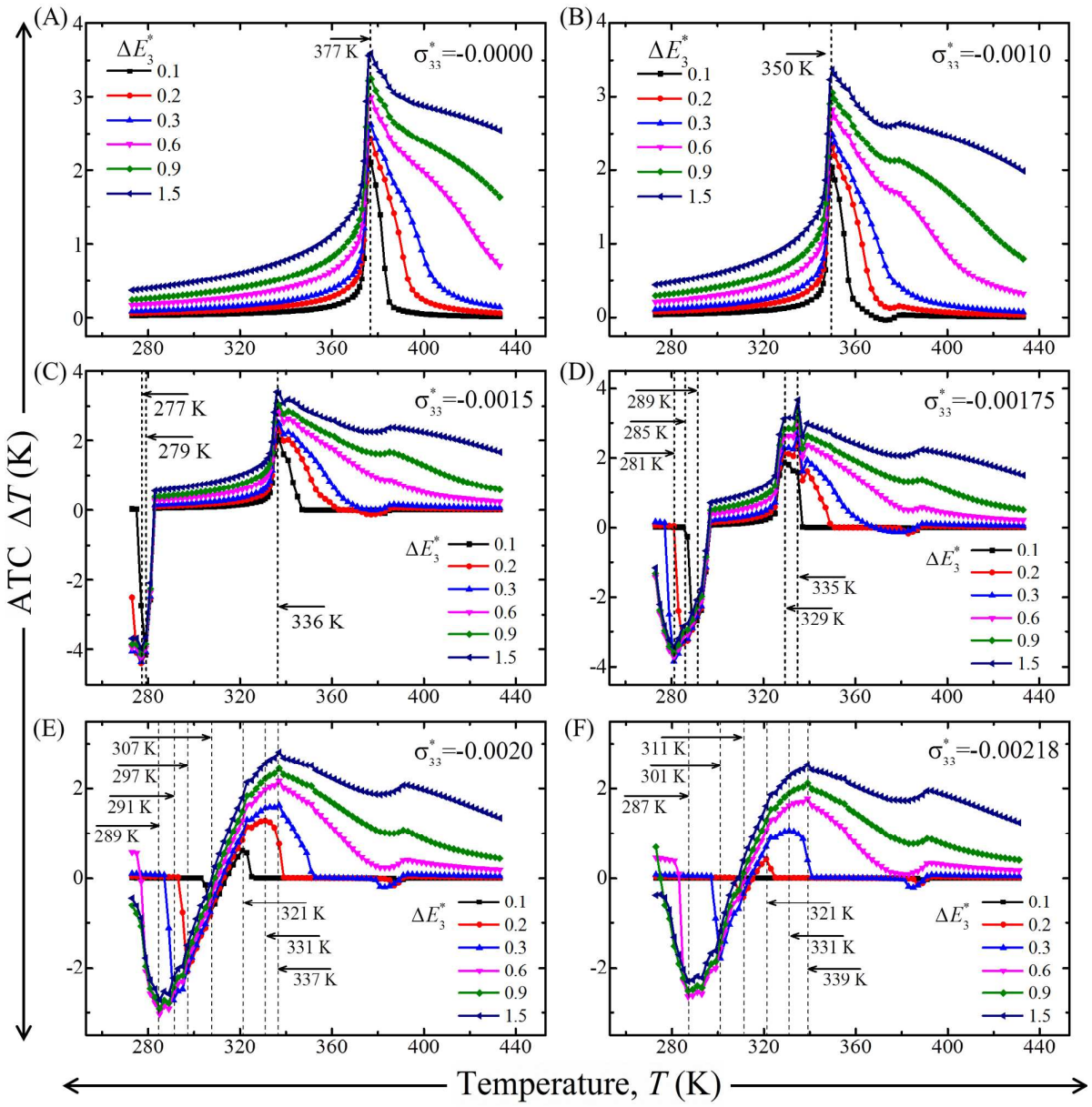

Fig. 8 ATC ΔT as a function of temperature under sustained compression: (A) σ_{33}^*=0, (B) σ_{33}^* =-0.001, (C) σ_{33}^*=-0.0015, (D) σ_{33}^*=-0.00175, (E) σ_{33}^*=-0.002, (F) σ_{33}^*=-0.00218. The dash lines indicate the peak of EFIPPT temperature under different external electric field ΔE_3^*.

Graphical Table of Contents

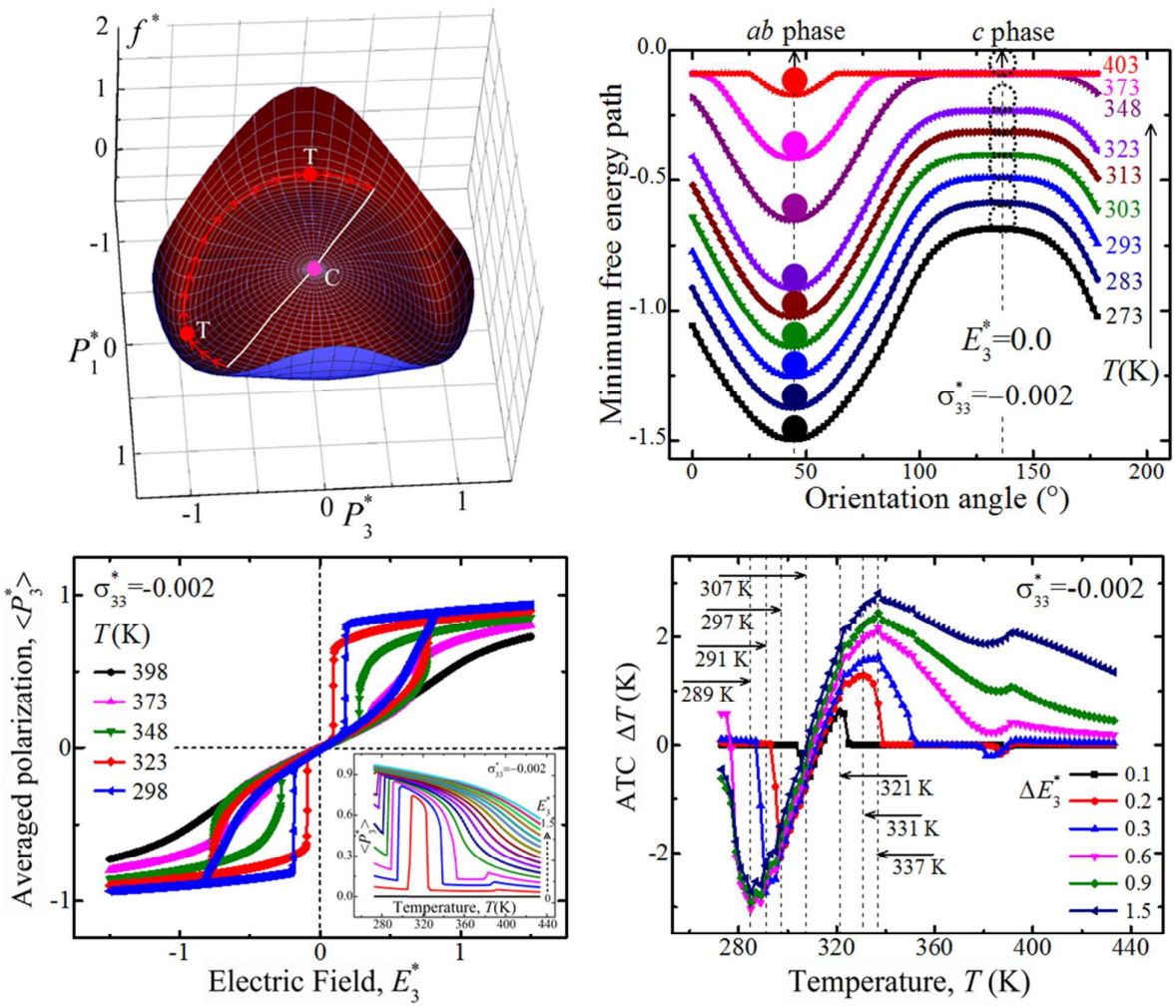

The double polarization-electric-field hysteresis loops are signals of the coexistence of positive and negative EC effects in one tetragonal ferroelectric material. The ATC peak temperature can be tuned by external electric field and mechanical compression. These new findings will pave a completely new way for the application of ferroelectric materials in solid cooling devices.